Customized Fading Scaffolds: Strong Polyorthoester Networks via Thiol-ene Crosslinking for Cytocompatible Surface-Eroding Materials in 3D Printing

*Gordon Herwig,[a,b,c] Maria M. Pérez-Madrigal[b] and Andrew P. Dove[b,] ***

[a]Department of Chemistry, University of Warwick, Coventry, CV8 4AL, UK

[b]School of Chemistry, University of Birmingham, Edgbaston, Birmingham, B15 2TT, UK

[c]Laboratory for Advanced Fibers, Empa - Swiss Federal Laboratories for Materials Testing and Research, Lerchenfeldstrasse 5, 9014 St. Gallen, CH

ABSTRACT

Polyorthoesters are a highly desirable class of cytocompatible materials that are able to rapidly surface-erode. Despite their promise, their mechanical weakness and complex synthesis have limited their processability and application in advanced technologies. Herein we report a readily accessible family of crosslinked poly(orthoester-thioether) (POETE) materials that are suitable for processing *via* photopolymerization. Polymer networks are accessed through bifunctional orthoester (OE) precursors using simple thiol-ene addition chemistry. The mobility of the polymer chains and crosslinking density within the polymer structure can be tuned through the choice of monomer, which in turn presents customizable thermal and mechanical properties in the resulting materials. The photopolymerizability of these POETE materials also allows for processing *via* additive manufacturing, which is demonstrated on a commercial 3D printer. Post-processing conditions and architecture are crucial to material degradability and are exploited for programmed bulk-release applications with degradation rate and release time linearly dependent on the specimen dimensions, such as strand or shell thickness. Analogous to acid-releasing polylactide materials, degradation products of the POETE materials show cytocompatibility below a certain concentration/acidity threshold. This research highlights the simplicity, versatility and applicability of POETE networks as cytocompatible, surface-eroding materials that can be processed by additive manufacturing for advanced applications.

INTRODUCTION

Additive manufacturing (AM) has been an essential scalable industrial technique in rapid prototyping for decades[1] that now finds application in engineering,[2] architecture[3] and medicine.[4-5] Typically, the process comprises of the 3D printing of a computer-aided design (CAD), followed by post treatment, such as thermal or photo-based post-curing and

functionalization.[6] Such methods are able to achieve structures with high levels of complexity and accuracy, as well as a decreased number of production steps compared to ordinary molding techniques.[7] Among the 3D printing techniques suitable for polymers (*e.g.* thermal processes like Fused Filament Fabrication (FFF/FDM) and photochemical processes, such as Stereolithography (SLA) and Digital Light Processing (DLP)), light-based techniques produce objects of superior detail and integrity as a consequence of the high-precision light-induced crosslinking on a molecular level. The whole-layer approach of DLP leads to shorter curing intervals and manufacturing duration overall, which renders it ideal for sensitive or degradable materials and truly rapid prototyping. Indeed, DLP produces masters in indirect manufacturing,[8] and has been established as the leading technique in guides for surgical orthopedics.[9]

Materials based on polylactic acid (PLA), polycaprolactone (PCL), polycarbonate (PC), poly(ethyl ether ketone) (PEEK), polyethylene terephthalate (PET), Nylon, polystyrene (PS), and polyglycolic acid (PGA) have been widely studied as biomaterials and have been the focus of extensive research for application in AM in recent years.[4-5, 10-19] With most focus on adapting these materials for FFM/FDM, the low biocompatibility of leachable additives, diluents, or plasticizers, in combination with the limited mechanical parameters of these materials as well as their largely bulk erosion profiles makes them non-ideal for wider biomedical application. Hence, in order to expand the current library of suitable resources, more advanced materials are needed to address these limitations. To this end, the focus of this work has been placed on the design of new polymer systems with inherent surface erosion properties and mechanical properties that can be readily tuned across a wide parameter space that will lead to a customizable material that can be processed using advanced, AM processes for not only biomedical applications,[20] but also technological and energetic purposes, such as for structural models and intricately designed accessories and devices. For instance, strong surface-erodible materials provide stability and a controlled degradation over time as 3D

printed scaffolds or drug delivery vehicles.[21] Hydrolytic degradation behavior can be estimated based on the relation between reactivity of polymeric bonds, diffusion through the matrix and dimensions of a sample.[22]

The most common classes of surface-erodible materials used in biomedical research, for example, include polyanhydrides,[23-24] polyacetals[25] and polyorthoesters (POEs),[26] and some aliphatic polycarbonates[27] and specific long-chain acids.[28-30] Unfortunately, generally, these materials lack the ability to be manufactured quickly, 3D printed and efficiently with tailored features for a specific application or by photochemical means that enable 3D printing. Attempts to synthesize biomaterials that are both photopolymerizable and surface-erodible have been limited. While studies have shown that photocrosslinked poly(glycerol sebacate) (PGS) and poly(propylene fumarate) (PPF) display surface erosion properties in the presence of enzymes,[31-32] polymer families that are simply hydrolytically surface eroding are even fewer. Polyanhydride-copolymers provide a potential route, however the study of these materials is often limited by high local acidity on the surfaces upon degradation, sensitivity to oxygen and moisture during the manufacturing process, or limited mechanical diversity.[33] Surface erodible POEs, as first reported by Heller *et al.*,[34] degrade mainly into alcohols and water soluble, small molecule acids[35] and have already been studied for potential biomedical applications.[35-36] However, difficult synthesis and inferior mechanical properties have prevented their wider application to date.[37-38] Even recent polyorthoester amide and urethane polymers require harsh polymerization conditions and exhibit no significant mechanical strength, thus not being adequate for rapid prototyping purposes.[39-40]

In previous work,[41] we presented a simple and versatile method to synthesize orthoester- and acetal-based polymers using 2-methylene-1,3-dioxe-5-pene as a stable bifunctional monomer. The resulting linear poly(orthoester-thioether)s or poly(acetal-thioether)s possessed a weight-average molecular weight of above 10 kg·mol^{-1} and displayed surface-erosion

4

behavior. Herein, we explore the application of this platform to create novel poly(orthoester-thioether)s (POETEs) through thiol-ene radical coupling reactions for AM applications. The comprehensive manufacturing process allowed for a customizable linker composition and network structure, while the molecular architecture provided access to a diverse new library of materials that can act as supports or surface-erodible 3D printed devices.

EXPERIMENTAL SECTION

Materials

Acetone (Fisher), Aliquat 336 (Sigma-Aldrich), basic aluminium oxide (Sigma-Aldrich), 1,4-benzenedimethanol (Alfa Aesar), 2-bromo-1,1-dimethoxyethane (Acros Organics), 2-butyne-diol (Sigma-Aldrich), *cis*-2-butene-1,4-diol (Sigma-Aldrich), diethyl ether (Sigma-Aldrich), dipentaerythritol hexa(3-mercaptopropionate) (**6SH**) (Bruno Bock Chemische Fabrik GMBH & Co.KG), 1,6-hexanediol (Sigma-Aldrich), hydrochloric acid (37%, Fisher Scientific), hydroquinone (Sigma-Aldrich), Irgacure 819 (IGM Resins Ltd.), pentaerythritol tetrakis(3-mercaptopropionate) (**4SH**) (Sigma-Aldrich), phosphate buffered saline preparation (Sigma-Aldrich), potassium carbonate (anhydrous, Sigma-Aldrich), potassium *tert*-butoxide (Sigma-Aldrich), 1,3-propanediol (Sigma-Aldrich), propylene carbonate (Alfa Aesar), terephthalic acid (Sigma-Aldrich), tetrahydrofuran (Sigma-Aldrich), *p*-toluenesulfonic acid (Sigma), trimethylolpropane tris(3-mercaptopropionate) (**3SH**) (Sigma-Aldrich) and sodium hydroxide (Sigma-Aldrich) were used as received from the supplier. Paprika extract (Durabrite, Kalsec) and food colorings (Tesco Stores Ltd.) were also used as received. CDCl$_3$ (Sigma-Aldrich) was stored over anhydrous potassium carbonate and plug filtered through basic aluminium oxide immediately before use. All glassware used for handling and storage of OE-containing compounds and liquid resins was silanized by treating the inner surface with Sigmacote

(Sigma-Aldrich) for five minutes, followed by rinsing with water, acetone, diethyl ether and subsequent drying under compressed air for one minute.

Methods

DSC and TGA thermograms were collected on a Mettler-Toledo STARe DSC/TGA 3+ system with STARe Excellence Thermal Analysis Software V2.22. DMTA studies were performed using a Mettler-Toledo Mettler Toledo DMA1 STAR-e device with the same software and, for oscillatory measurements, a common constant distance resulting in a maximum force of around 5 N for the strongest samples in the glassy state (CKA-4TE). Tensile testing was performed on a Testometric M350-5CT with environmental setup, 5 kgF load cell and adjustable manual grips at a rate of 4 mm·min^{-1} with an offset of 0.1 N while operated and analyzed *via* Win TestAnalysis (v.5.0.34) software. Nuclear Magnetic Resonance (NMR) spectra were acquired using a Bruker Avance III 300 or 400 MHz, processed by MestReNova software using the residual solvent peak as reference (CDCl$_3$, ^{1}H: δ = 7.26 ppm, ^{13}C: δ = 77.16 ppm). Mass spectra were obtained *via* a Bruker maXis plus. Elemental analysis was conducted on a CE Instruments EA1110 Elemental Analyser. An Agilent Cary 630 FTIR Spectrometer with Agilent Resolutions Pro software V.5.0 was used for IR spectroscopy. Raman spectroscopy was performed on a Renishaw inVia Reflex Raman Microscope using a 633 nm HeNe excitation laser and 20× objective. Oscillatory rheometry was performed on an Anton Parr MCR-302 with PP25 plates, Omnicure S1500 UV source and RheoCompass™ V1.20.496 software at a frequency of 10 Hz, amplitude of 1% and gap width of 0.2 mm.

Thickness-dependent cylinder erosion and release studies. Hollow cylindrical OE3-4TE samples were produced according to the synthesis described below. After measuring the lowest thickness and confirming the samples were free of rips and bubbles, Araldite 2-part

epoxy glue was mixed and added to one full edge, followed by pressing this side onto a silanized circular glass slide. After drying for 1 h, undiluted food coloring (blue, red and yellow - Tesco Stores Ltd.) was added into the well until the formed meniscus was approximately 2 mm away from the top rim. This edge was subsequently covered in a slightly more viscous epoxy-glue formulation and closed off with a silanized circular glass slide, while making sure not to leave any gap or weak spot. After drying for 1 h the samples were clipped into a self-made sample holder of copper wire, which was then fixated onto a 50 mL plastic tub. The tub was then filled with 40 mL of 1 M HCl and the time measurement started. A video was recorded at 59.94 fps and subsequently evaluated frame-by-frame *via* MATLAB to calculate the development of HSI-values over time for each sample solution. The onset of the change in Saturation (HSI) was used as time point for the release diagram.

Cytotoxicity of degradation products. To assess the cytotoxicity of OE3-4TE, cell viability tests on NOR-10 cells (ATCC® CCL-197™, mouse skeletal muscle fibroblasts) were undertaken. To that end, 100 mg of 3D printed and with concentrated acid treated OE3-4TE were immersed in 5 mL of cell culture media (DMEM-high glucose; 20% FBS; 1% pen/strep) at 37 °C for several days until complete dissolution (i.e. 20 mg/mL). Then, the cell media was recovered and filtered before being used. Because of the acidic nature of the degradation products, the pH of the cell media decreased and it displayed a light orange color. NOR-10 cells were cultured in 175 cm^2 tissue culture flasks using DMEM-high glucose (D6429-Sigma Aldrich), as advised by the supplier, with addition of 20% FBS and 1% pen/strep, at 37 °C, 5% CO_2. Cells were seeded on 24 well plates (5000 cells cm^{-2}) for viability assays. Cells were left to adhere and proliferate on the wells for 48 h, then incubated with the cell media containing the sample at six different concentrations, ranging from 20 mg/mL to 0.63 mg/mL. To evaluate the effect of the pH drop, cells were exposed also to cell media containing the sample but with neutral pH (increased by adding 10 uL of NaOH 1 M). Then, cell viability

was measured after 48 h of incubation using PrestoBlue® Cell Viability Reagent (InvitrogenTM). Experiments were performed in triplicate, and the results are reported as relative viability in comparison to the control (cell culture media without dissolved sample). Cell viability was also assessed using Live/DeadTM Viability/Cytotoxicity Kit (InvitrogenTM), which includes calcein AM for live cells ($\lambda_{Ex.}$ = 495, $\lambda_{Em.}$ = 515) and ethidium homodimer for dead cells ($\lambda_{Ex.}$ = 528, $\lambda_{Em.}$ = 617). The staining solution was prepared by dissolving calcein AM (0.5 μL mL^{-1}) and ethidium homodimer (2 μL mL^{-1}) in PBS and incubated with the samples for 30 minutes. Samples were imaged using an Olympus Confocal Laser Scanning Microscope (Fluoview FV3000) at 4X magnification and excited using the 488 and 561 nm lasers. Images were processed using CellSens (Olympus) and ImageJ software (1.52i).

XPS studies. X-ray photoelectron spectroscopy (XPS) data were collected using an Omicron Multiprobe instrument at the University of Warwick Photoemission Facility. The samples investigated in this study were mounted on Omicron sample plates using conductive carbon tape and loaded in to the fast-entry chamber. Once a pressure of less than 1×10^{-7} mbar had been achieved (*c.a.* 1 h), the samples were transferred to a 12-stage storage carousel, located between the preparation and main analysis chambers, for storage at pressures of less than 2×10^{-10} mbar. XPS measurements were conducted in the main analysis chamber (base pressure 2×10^{-11} mbar), with the sample being illuminated using an XM1000 monochromatic Al kα x-ray source (Omicron Nanotechnology). The measurements were conducted at room temperature and at a take-off angle of 90°. The photoelectrons were detected using a SPHERA electron analyzer (Omicron Nanotechnology), with the core level spectra recorded using a pass energy of 10 eV (resolution approx. 0.47 eV). The data were analyzed using the CasaXPS package, using Shirley backgrounds, mixed Gaussian-Lorentzian (Voigt) line shapes

and asymmetry parameters where appropriate. Due to the insulating nature of the samples, the surfaces became positively charged during the experiment. To compensate for this, a low energy electron gun was used to negate surface charging effects and the spectra were energy-corrected using the main C-C/C-H component in the C 1s region at 284.6 eV.

Synthesis of 2-(bromomethyl)-1,3-dioxe-5-pene (BrCKA). The procedure follows a method described by Plikk et al.[42] *Cis*-2-butene-1,4-diol (33.30 g, 378 mmol) and 2-bromo-1,1-dimethoxyethane (63.89 g, 378 mmol) were weighed into a 100 mL round bottom flask, followed by p-toluenesulfonic acid (0.10 g, 0.1 wt%). A stirrer bar, Vigreux condenser and distillation bridge was added and the mixture incrementally heated to 130 °C under stirring, until no more methanol was distilled over. After cooling to room temperature and gradually reducing the pressure, a residual methanol fraction was discarded and subsequently the pure product distilled at 38-42 °C and 0.05 mbar (62.1 g, 85%). Characterized as reported previously.[42] ^{1}H NMR (400 MHz; 298 K; CDCl$_3$): δ 5.70 (t, $^{3}J_{HH}$ = 1.5 Hz, 2H), 4.97 (t, $^{3}J_{HH}$ = 5.4 Hz, 1H), 4.44 (dm, $^{3}J_{HH}$ = 14.7 Hz, 2H), 4.20 (dm, $^{3}J_{HH}$ = 14.7 Hz, 2H), 3.39 (d, $^{3}J_{HH}$ = 5.4 Hz, 2H); ^{13}C NMR (400 MHz; 298 K; CDCl$_3$): δ 128.81, 106.92, 63.25, 24.99.

*Synthesis of 2-methylene-1,3-dioxe-5-pene (**CKA, 1**).* Similarly to Plikk et al.'s method,[42] BrCKA (40.00 g, 207 mmol) and Aliquat 336 (1.62 g, 4 mmol) were weighed into a 500 mL RBF, dissolved in 350 mL THF and cooled under stirring to 0 °C. Potassium *tert*-butoxide (46.50 g, 414 mmol) was added in small portions within 1 h and the orange to yellow suspension left to stir for another 2 h at 0 °C. THF was removed *in vacuo* (20 mbar, 18 °C) and the residual slurry dissolved in 200 mL diethyl ether and 200 mL distilled water, followed by separation of the layers and extraction of the aqueous phase with a further 100 mL diethyl ether. The combined organic layers were washed with 0.01 M potassium carbonate solution (3x, 300 mL). The organic layer was concentrated *in vacuo* at 18 °C, followed by vacuum transfer of the residual oil at room temperature and 0.05 mbar to yield crude product. Repeat

of the washing procedure, followed by drying over potassium carbonate and concentration at 30 °C and 20 mbar yielded pure product (12.50 g, 55%). ^{1}H NMR (400 MHz; 298 K; CDCl$_3$): δ 5.72 (t, $^3J_{HH}$ = 1.7 Hz, 2H), 4.43 (d, $^3J_{HH}$ = 1.7 Hz, 4H), 3.57 (s, 2H); ^{13}C NMR (400 MHz; 298 K; CDCl$_3$): δ 164.11, 127.83, 68.77, 68.21.

General procedure of the orthoester (OE) synthesis (2). CKA **(1)** and diol were weighed into a silanized vial in a molar ratio of 1.05 to 0.5. Terephthalic acid (1 mol equiv) was added and the mixture stirred overnight. The crude product was dissolved in 5 equiv v/v diethyl ether and washed with 0.01 M potassium carbonate solution (4x, 5 equiv v/v), followed by separation and drying of the organic layer over potassium carbonate. Plug filtration through minimal amounts of basic alumina and evaporation yielded pure OE product of a fruity odor *(2)*. Additional distillation *in vacuo* in a silanized setup before use was performed to remove any degradation products (around ^{1}H NMR δ = 2.00 ppm).

Synthesis of 1,3-bis(2-methyl-2-oxyl-1,3-dioxe-5-pene)-propane (OE3, 2a). CKA **(1)** (10.00 g, 89.18 mmol), 1,3-propanediol (3.40 g, 44.59 mmol) and terephthalic acid (0.15 g, 0.89 mmol) were reacted to yield clear colorless oil (11.20 g, 84%; distillation at 0.02 mbar, 150 °C). ^{1}H NMR (400 MHz; 298 K; CDCl$_3$): δ 5.66 (t, $^3J_{HH}$ = 1.7 Hz, 4H, -C*H*CH$_2$CO$_3$-), 4.43 (dm, 4H, $^2J_{HH}$ = -15.5 Hz, -CHC*H*$_2$CO$_3$-), 4.15 (dm, 4H, $^2J_{HH}$ = -15.5 Hz, -CHC*H*$_2$CO$_3$-), 3.65 (t, 4H, $^3J_{HH}$ = 6.3 Hz, -OC*H*$_2$CH$_2$-), 1.93 (qi, 2H, $^3J_{HH}$ = 6.3 Hz, -OCH$_2$C*H*$_2$-), 1.54 (s, 6H, -CO$_3$C*H*$_3$); ^{13}C NMR (400 MHz; 298 K; CDCl$_3$): δ 128.99 (-*C*HCH$_2$CO$_3$-), 116.20 (-*C*O$_3$CH$_3$), 61.57 (-CH*C*H$_2$CO$_3$-), 60.42 (-CO$_3$*C*H$_2$CH$_2$-), 30.37 (-CO$_3$CH$_2$*C*H$_2$-), 19.18 (-CO$_3$*C*H$_3$); MS (ESI-QTOF +ve): (M + Na)$^+$ *m/z* calculated for C$_{15}$H$_{24}$O$_6$Na$^+$: 323.1465, found: 323.1468; Anal. Calcd for C$_{15}$H$_{24}$O$_6$: C 60.0; H 8.05%. Found: C 59.9; H 8.0; IR (neat; 298 K; cm^{-1}): 2950-2860 (-C-H), 1380 (-CH$_2$-), 1160-1040 (C-O), 900 (-CH$_2$-CH$_2$-), 800

(C=C), 640 (=C-H); Raman (neat; 298 K; cm^{-1}): 3030 (=C-H), 2950-2870 (C-H), 1660 (C=C), 1450 (-CH$_2$-), 1200 (C-C), 750 (C-O).

Synthesis of 1,6-bis(2-methyl-2-oxyl-1,3-dioxe-5-pene)-hexane **(OE6, 2b)**. CKA **(1)** (10.00 g, 89.18 mmol) was combined with 1,6-hexanediol (5.27 g, 44.59 mmol) and terephthalic acid (0.15 g, 0.89 mmol), reacted and clear oil was obtained (12.52 g, 82%). ^{1}H NMR (300 MHz; 298 K; CDCl$_3$): δ 5.66 (s, 4H, -OCH$_2$C$_2$H$_2$CH$_2$O-), 4.43 (d, 4H, $^2J_{H-H}$ = -14.1 Hz, -OCH$_2$C$_2$H$_2$CH$_2$O-), 4.43 (d, 4H, $^2J_{H-H}$ = -14.1 Hz, -OCH$_2$C$_2$H$_2$CH$_2$O-), 3.50 (t, 4H, $^3J_{H-H}$ = 6.6 Hz, -OCH$_2$CH$_2$CH$_2$-), 1.62 (tm, 4H, $^3J_{H-H}$ = 6.7 Hz, -OCH$_2$CH$_2$CH$_2$-), 1.52 (s, 6H, -CH$_3$) , 1.42 (q, 2H, $^3J_{H-H}$ = 3.8 Hz, -OCH$_2$CH$_2$CH$_2$-); ^{13}C NMR (300 MHz; 298 K; CDCl$_3$): δ 129.03 (-OCH$_2$C$_2$H$_2$CH$_2$O-), 116.17 (-O$_3$CCH$_3$), 63.42 (-OCH$_2$C$_2$H$_2$CH$_2$O-), 61.54 (-OCH$_2$CH$_2$CH$_2$-), 29.96 (-OCH$_2$CH$_2$CH$_2$-), 26.23 (-OCH$_2$CH$_2$CH$_2$-), 19.18 (-CH$_3$); MS (ESI-QTOF +ve): (M + Na)$^+$ *m/z* calculated for C$_{18}$H$_{30}$O$_6$Na$^+$: 365.1935, found: 365.1935; Anal. Calcd for C$_{18}$H$_{30}$O$_6$: C 63.1; H 8.8%. Found: C 62.9; H 8.9; IR (neat; 298 K; cm^{-1}): 2940-2860 (-C-H), 1380 (-CH$_2$-), 1210-1010 (C-O), 900 (-C-H), 800 (C=C), 640 (=C-H); Raman (neat; 298 K; cm^{-1}): 3040 (=C-H), 2950-2870 (C-H), 1660 (C=C), 1450 (-CH$_2$-), 1200 (C-C), 750 (C-O).

Synthesis of 1,4-bis((2-methyl-1,3-dioxe-5-pene-2-yl)oxymethyl)-benzene **(OEbz, 2c)**. Acetone (10 mL) was added to CKA **(1)** (10.00 g, 89.18 mmol), 1,4-bis(hydroxymethyl)-benzene (6.16 g, 44.59 mmol) and terephthalic acid (0.15g, 0.89 mmol), and the mixture was reacted to yield white crystals. (11.69 g, 72%; recrystallization from diethyl ether, drying *in vacuo* from melt). Mp. 95-98 °C; ^{1}H NMR (300 MHz; 298 K; CDCl$_3$): δ 7.32 (s, 4H, -C$_6$H$_4$-), 5.63 (s, 4H, -OCH$_2$C$_2$H$_2$CH$_2$O-), 4.58 (s, 4H, -OCH$_2$C$_6$H$_4$-), 4.44 (d, 4H, $^2J_{H-H}$ = -15.5 Hz, -OCH$_2$C$_2$H$_2$CH$_2$O-), 4.12 (d, 4H, $^2J_{H-H}$ = -15.5 Hz, -OCH$_2$C$_2$H$_2$CH$_2$O-), 1.58 (s, 6H, -CH$_3$); ^{13}C NMR (400 MHz; 298 K; CDCl$_3$): δ 137.49 (-OCH$_2$CC$_4$H$_4$CCH$_2$O-), 128.96 (-OCH$_2$C$_2$H$_2$CH$_2$O-), 127.58 (-OCH$_2$CC$_4$H$_4$CCH$_2$O-), 116.53 (-O$_3$CCH$_3$), 65.51

(-OCH_2C$_6$H$_4$-), 61.78 (-O$CH_2$$C_2H_2CH_2$O-), 19.58 (-$CH_3$); MS (ESI-QTOF +ve): (M + Na)$^+$ m/z calculated for $C_{20}H_{26}O_6Na^+$: 385.1622, found: 385.1622; Anal. Calcd for $C_{20}H_{26}O_6$: C 66.3; H 7.2%. Found: C 66.4; H 7.3; IR (neat; 298 K; cm^{-1}): 2960-2860 (-C-H), 1380 (-CH$_2$-), 1210-1010 (C-O), 920-900 (-C-H), 830-770 (C=C), 650 (=C-H); Raman (neat; 298 K; cm^{-1}): 3070-3040 (=C-H), 2960-2860 (C-H), 1660 (C=C), 1460 (-CH$_2$-), 1200-1180 (C-C), 760 (C-O).

*Synthesis of 1,4-bis((2-methyl-1,3-dioxe-5-pene-2-yl)oxy)-benzene (**OEph, 2d**)*. Analogous to (**2c**), dissolving CKA (**1**) (10.00 g, 89.18 mmol), benzene-1,4-diol (4.91 g, 44.59 mmol) and terephthalic acid (0.15 g, 0.89 mmol) in acetone (10 mL) and reacting yielded the product as white platelets (10.66, 71%; recrystallization from diethyl ether). Mp. 105-108 °C; ^{1}H NMR (300 MHz; 298 K; CDCl$_3$): δ 7.06 (s, 4H, -C$_6$H$_4$-), 5.72 (s, 4H, -OCH$_2$C$_2$$H_2CH_2$O-), 4.62 (d, 4H, $^2J_{\text{H-H}}$ = -15.5 Hz, -OCH_2C$_2$H$_2$CH$_2$O-), 4.25 (d, 4H, $^2J_{\text{H-H}}$ = -15.5 Hz, -OCH$_2$C$_2$H$_2$CH_2O-), 1.54 (s, 6H, -CH_3); ^{13}C NMR (400 MHz; 298 K; CDCl$_3$): δ 149.91 (-OCC_4H$_4$CO-), 128.81 (-OCH$_2$$C_2H_2CH_2$O-), 121.79 (-OC$C_4H_4$CO-), 117.85 (-O$_3$$CCH_3$), 62.17 (-O$CH_2C_2H_2CH_2$O-), 20.02 (-$CH_3$); MS (ESI-QTOF +ve): (M + Na)$^+$ m/z calculated for $C_{18}H_{22}O_6Na^+$: 357.1309, found: 357.1304; Anal. Calcd for $C_{18}H_{22}O_6$: C 64.7; H 6.6%. Found: C 64.9; H 6.65; IR (neat; 298 K; cm^{-1}): 2950-2870 (-C-H), 1500 (C=C), 1380 (-CH$_2$-), 1210-1010 (C-O), 920-900 (-C-H), 840-780 (C=C), 640 (=C-H); Raman (neat; 298 K; cm^{-1}): 3080-3040 (=C-H), 2990-2950 (C-H), 1664 (C=C), 1250-1200 (C-C), 760 (C-O).

*Synthesis of cis-1,4-bis(2-methyl-2-oxyl-1,3-dioxe-5-pene)-but-2-ene (**OE4ene, 2e**)*. The reaction of CKA (**1**) (10.00 g, 89.18 mmol), *cis*-2-butene-1,4-diol (3.93 g, 44.59 mmol) and terephthalic acid (0.15 g, 0.89 mmol) yielded white crystals (2.25 g, 81%; recrystallization from diethyl ether). Mp. 24-26 °C; ^{1}H NMR (400 MHz; 298 K; CDCl$_3$): δ 5.71 (tm, $^3J_{\text{HH}}$ = 3.6 Hz, 2H, -CHCH$_2$CO$_3$- *(linker)*), 5.56 (t, $^3J_{\text{HH}}$ = 1.7 Hz, 4H, -CHCH$_2$CO$_3$-), 4.43 (dm, 4H,

$^2J_{HH}$ = -14.2 Hz, -CHCH_2CO$_3$-), 4.15 (d, 4H, $^3J_{HH}$ = 3.6 Hz, -CHCH_2CO$_3$- *(linker)*), 4.13 (dm, 4H, $^2J_{HH}$ = -14.2 Hz, -CHCH_2CO$_3$-), 1.54 (s, 6H, -CO$_3$CH_3); ^{13}C NMR (400 MHz; 298 K; CDCl$_3$): δ 128.94 (-CHCH$_2$CO$_3$-), 128.64 (-CHCH$_2$CO$_3$- *(linker)*), 116.35 (-CO$_3$CH$_3$), 61.70 (-CHCH$_2$CO$_3$-), 59.72 (-CHCH$_2$CO$_3$- *(linker)*), 30.37 (-CO$_3$CH$_2$CH$_2$-), 19.40 (-CO$_3$CH$_3$); MS (ESI-QTOF +ve): (M + Na)$^+$ *m/z* calculated for C$_{16}$H$_{24}$O$_6$Na$^+$: 335.1465, found: 335.1468; Anal. Calcd for C$_{16}$H$_{24}$O$_6$: C 61.5; H 7.7%. Found: C 61.5; H 7.8; IR (neat; 298 K; cm^{-1}): 2950-2860 (-C-H), 1380 (-CH$_2$-), 1140-1020 (C-O), 900 (-C-H), 800 (C=C), 640 (=C-H); Raman (neat; 298 K; cm^{-1}): 3050-3030 (=C-H), 2950-2880 (C-H), 1670-1660 (C=C), 1450 (-CH$_2$-), 1200 (C-C), 770 (C-O).

*Synthesis of 1,4-bis((2-methyl-2-oxyl-1,3-dioxe-5-pene)-but-2-yne (**OE4yne, 2f**).* Reacting CKA (**1**) (10.00 g, 89.18 mmol), benzene-1,4-diol (3.84 g, 44.59 mmol) and terephthalic acid (0.15 g, 0.89 mmol) yielded the product as fine white crystals (13.73 g, 99%; recrystallization from diethyl ether). Mp. 40-43 °C; ^{1}H NMR (300 MHz; 298 K; CDCl$_3$): δ 5.65 (s, 4H, -OCH$_2$C$_2$H$_2$CH$_2$O-), 4.46 (d, 4H, $^2J_{H-H}$ = -15.5 Hz, -OCH$_2$C$_2$H$_2$CH$_2$O-), 4.28 (s, 4H, -CH$_2$C$_2$CH$_2$-), 4.14 (d, 4H, $^2J_{H-H}$ = -15.5 Hz, -OCH$_2$C$_2$H$_2$CH$_2$O-), 1.56 (s, 6H, -CH$_3$) ; ^{13}C NMR (400 MHz; 298 K; CDCl$_3$): δ 128.83 (-OCH$_2$C$_2$H$_2$CH$_2$O-), 116.55 (-O$_3$CCH$_3$), 81.93 (-CH$_2$C$_2$CH$_2$-), 61.90 (-OCH$_2$C$_2$H$_2$CH$_2$O-), 52.12 (-CH$_2$C$_2$CH$_2$-), 19.50 (-CH$_3$); MS (ESI-QTOF +ve): (M + Na)$^+$ *m/z* calculated for C$_{16}$H$_{22}$O$_6$Na$^+$: 333.1309, found: 333.1317; Anal. Calcd for C$_{16}$H$_{22}$O$_6$: C 61.9; H 7.15%. Found: C 61.9; H 7.0; IR (neat; 298 K; cm^{-1}): 2960-2870 (-C-H), 1390-1360 (-CH$_2$-), 1150-990 (C-O), 900 (-C-H), 800 (C=C), 650 (=C-H); Raman (neat; 298 K; cm^{-1}): 3030 (=C-H), 2960-2870 (C-H), 1660 (C=C), 1450 (-CH$_2$-), 1200 (C-C), 750 (C-O).

*Preparation of P(OE-TE) materials (**3**).* The melt of the respective OE monomer and thiol linker in a 1:1 ratio of thiol to cyclic alkene functionalities together with 1.0 wt% total of the initiator was stirred in an amber silanized vial for 10 minutes until homogeneous. A stainless-

steel mold, featuring cut-out dog-bone shapes for tensile testing and bars for DMA testing, was one-sidedly covered with Sellotape and filled with the mixture. Alternatively, a clear plastic template made from a 5mL PP syringe with a parafilm-wrapped core or a 2 mL PP vial cap was used for hollow cylinders and degradation pucks, respectively. Photocuring was performed in an NK-Optik Otoflash G171 applying 500 flashes/cycle for 8 cycles, followed by extraction of the materials from the mold and further curing (500 flashes/cycle for 4 cycles), cooling the sample to room temperature in between each cycle for quasi-isothermal curing conditions. Post-curing was conducted at 120 °C either (a) *in vacuo* at $\leq 5 \cdot 10^{-2}$ mbar after purging with nitrogen or (b) in an ambient atmosphere using a hot plate or ventilated oven. In between experiments, all samples were stored at −25 °C.

Preparation of OE3-3TE (3a$_1$). A mixture of OE3 **(2a)** (1.00 g, 3.33 mmol), 3SH (0.89 g, 1.66 mmol) and Irgacure 819 (0.02 g, 1 wt%) were prepared in a silanized glass vial and reacted to form a clear, colorless polymer. IR (neat; 298 K; cm^{-1}): 2950-2880 (-C-H), 1730 (C=O), 1460-1360 (-CH$_2$-), 1240-1140 (C-O), 1050-1020 (C-O), 910 (-C-H); Raman (neat; 298 K; cm^{-1}): 2940 (C-H), 1730 (C=O), 1460-1430 (-CH$_2$-), 1060 (C-O-C), 750 (C-O).

Preparation of OE3-4TE (3a$_2$). OE3 **(2a)** (1.00 g, 3.33 mmol), 4SH (0.81 g, 1.66 mmol) and Irgacure 819 (0.02 g, 1 wt%) were mixed in a silanized glass vial and polymerized into a clear, colorless material. IR (neat; 298 K; cm^{-1}): 2950-2880 (-C-H), 1730 (C=O), 1470-1360 (-CH$_2$-), 1240-1140 (C-O), 1030 (C-O); Raman (neat; 298 K; cm^{-1}): 2940 (C-H), 1740 (C=O), 1460-1430 (-CH$_2$-), 750 (C-O).

Preparation of OE3-6TE (3a$_3$). OE3 **(2a)** (1.00 g, 3.33 mmol), 6SH (0.87 g, 1.66 mmol) and Irgacure 819 (0.02 g, 1 wt%) were combined for the mixture and brought to reaction to form a clear, colorless polymer. IR (neat; 298 K; cm^{-1}): 2950-2880 (-C-H), 1730 (C=O), 1460-1350

(-CH$_2$-), 1240-1140 (C-O), 1050-1020 (C-O), 910 (-C-H); Raman (neat; 298 K; cm^{-1}): 2940 (C-H), 1740 (C=O), 1460-1430 (-CH$_2$-), 750 (C-O).

Preparation of OE6-4TE (3b). A mixture of OE6 **(2b)** (1.00 g, 2.92 mmol), 4SH (0.71 g, 1.46 mmol) and Irgacure 819 (0.02 g, 1 wt%) was prepared for the material to afford a clear, colorless polymer. IR (neat; 298 K; cm^{-1}): 2940-2870 (-C-H), 1730 (C=O), 1460-1350 (-CH$_2$-), 1240-1140 (C-O), 1050-1010 (C-O), 910 (-C-H); Raman (neat; 298 K; cm^{-1}): 2940 (C-H), 1740 (C=O), 1450-1430 (-CH$_2$-), 750 (C-O).

Preparation of OEbz-4TE (3c). The clear, colorless material was prepared by reacting OEbz **(2c)** (1.00 g, 2.76 mmol), 4SH (0.671 g, 1.38 mmol) and Irgacure 819 (0.02 g, 1 wt%) at 120 °C. IR (neat; 298 K; cm^{-1}): 2950-2870 (-C-H), 1730 (C=O), 1510 (-HC=CH-), 1470-1350 (-CH$_2$-), 1230-1130 (C-O), 1010 (C-O), 920 (-C-H), 810 (=C-H); Raman (neat; 298 K; cm^{-1}): 3060 (=C-H), 2930 (C-H), 1740 (C=O), 1620 (C=C), 1460-1420 (-CH$_2$-), 1200 (C-O), 840 (=C-H).

Preparation of OEph-4TE (3d). The photo-reaction between OEph **(2d)** (1.00 g, 2.99 mmol), 4SH (0.73 g, 1.50 mmol) and Irgacure 819 (0.02 g, 1 wt%) was conducted at 120 °C and yielded the brown, clear material. IR (neat; 298 K; cm^{-1}): 2960-2910 (-C-H), 1730 (C=O), 1510 (-HC=CH-), 1470-1360 (-CH$_2$-), 1230-1130 (C-O), 1030 (C-O), 830 (=C-H); Raman (neat; 298 K; cm^{-1}): 3070 (=C-H), 2940 (C-H), 1740 (C=O), 1620 (C=C), 1460-1420 (-CH$_2$-), 830-860 (=C-H).

Preparation of OE4ene-4TE (3e$_1$). The mixture was prepared with OE4ene **(2e)** (1.00 g, 3.20 mmol), 4SH (0.78 g, 1.60 mmol) and Irgacure 819 (0.02 g, 1 wt%) and a clear, colorless polymer was obtained. IR (neat; 298 K; cm^{-1}): 2950-2880 (-C-H), 1730 (C=O), 1470-1350 (-CH$_2$-), 1230-1130 (C-O), 1020 (C-O), 910 (-C-H); Raman (neat; 298 K; cm^{-1}): 2930 (C-H), 1740 (C=O), 1450-1420 (-CH$_2$-).

Preparation of OE4ene-4TE, full conversion (3e₂). Clear, colorless material was formed by the reaction of OE4ene **(2e)** (1.00 g, 3.20 mmol), 4SH (1.17 g, 2.40 mmol) and Irgacure 819 (0.02 g, 1 wt%). IR (neat; 298 K; cm⁻¹): 2950-2880 (-C-H), 1730 (C=O), 1470-1350 (-CH₂-), 1230-1130 (C-O), 1030 (C-O); Raman (neat; 298 K; cm⁻¹): 2930 (C-H), 1740 (C=O), 1660 (C=O), 1450-1420 (-CH₂-), 750 (C-O).

Preparation of OE4yne-4TE (3f₁). At 50 °C, OE4yne **(2f)** (1.00 g, 3.22 mmol), 4SH (0.79 g, 1.61 mmol) and Irgacure 819 (0.02 g, 1 wt%) were reacted to yield a clear, colorless polymer. IR (neat; 298 K; cm⁻¹): 2950-2880 (-C-H), 1730 (C=O), 1460-1350 (-CH₂-), 1240-1130 (C-O), 1020 (C-O), 910-900 (-C-H); Raman (neat; 298 K; cm⁻¹): 2940 (C-H), 1740 (C=O), 1660 (C=O), 1450-1420 (-CH₂-), 750 (C-O).

Preparation of OE4yne-4TE, full conversion (3f₂). A mixture of OE4yne **(2f)** (1.00 g, 3.22 mmol), 4SH (1.58 g, 3.22 mmol) and 0.03 g (1 wt%) Irgacure 819 was prepared at 50 °C and a clear, colorless polymer was obtained. IR (neat; 298 K; cm⁻¹): 2950-2930 (-C-H), 1730 (C=O), 1470-1350 (-CH₂-), 1230-1140 (C-O), 1020 (C-O), 920 (-C-H); Raman (neat; 298 K; cm⁻¹): 2930 (C-H), 2570 (-SH:HS-), 1740 (C=O), 1460-1420 (-CH₂-).

Preparation of CKA-4TE (4). A mixture of CKA **(1)** (1.00 g, 8.92 mmol), 4SH (2.18 g, 4.46 mmol) and 0.03 g (1 wt%) Irgacure 819 was prepared at 50 °C and a clear, colorless polymer was obtained. IR (neat; 298 K; cm⁻¹): 2940-2880 (-C-H), 1730 (C=O), 1470-1350 (-CH₂-), 1230-1120 (C-O), 1030-1000 (C-O); Raman (neat; 298 K; cm⁻¹): 2930-2920 (C-H), 1740 (C=O), 1460-1420 (-CH₂-).

Preparation and printing of 3D printing resin. OE3 **(2a)** (10.00 g, 33.29 mmol), 4SH (8.13 g, 16.65 mmol), propylene carbonate (9.07 g, 50 wt%) and equal masses of Irgacure 819 and Durabrite Paprika Extract (0.09 g, 0.5 wt% each) were weighed into an amber silanized bottle in a dark room. The mixture was stirred in the dark at ambient temperature until homogeneous

and clear, which occasionally required short exposure to ambient lighting. The resin was stored in the dark at 25 °C until further use. For stereolithography using a MiiCraft Ultra 50x (BURMS - 3D Druck Jena GmbH & Co.KG, Germany), a printing tray was filled with about 25 mL of resin and locked into place, which was usable for approximately 5 h of printing until insufficient photoinitiated curing occurred. After that, no solid material was formed as a consequence of hydrolysis and separation from hygroscopic effects, except *via* post-curing. Alternatively, approximately 3 mL of resin could be used at a time on the build plate and rearranged after every 5 to 10 printing steps, while topping up the batch regularly and completely replacing after around 5 h. The preset "slow" printing setup was selected with a modified step size of 100 (stents) or 200 µm (cuboid) as well as intensity of 350% and irradiation time of 14 s. 3 Base layers, at 24 s each, and 4 buffer layers were set up and the model offset from the base plate adjusted so that it was printed transition-free. The prints were further cured for 2 h in an NK-Optik G136/6 and a further 4×500 flashes in an NK-Optik Otoflash G171, before being post-cured in the oven. Finally, the timed erosion was achieved by placing the samples in concentrated (37%) HCl for 15-30 min, followed by rinsing in distilled water and peeling-off of solidified residual layers to reveal the self-wetting, surface-eroding stable material.

RESULTS AND DISCUSSION

Synthesis and preparation of networks

All synthesized materials are based on a cyclic ketene acetal (**Scheme 1** and **2**, compound **1**, CKA), which was obtained according to the procedure by Plikk *et al.*[42] *via* ring formation from bromoacetaldehyde dimethyl acetal, followed by dehydrohalogenation. Orthoester precursors (OEs, **2a-f**) were synthesized *via* addition reaction to different bifunctional alcohols. The resulting bifunctional OEs contained linkers with aliphatic chains of different

lengths (**2a, 2b**), aromatic groups (**2c, 2d**) and unreacted unsaturated bonds (**2e, 2f**) in order to investigate the effect of the linker structure on the chemical and physical properties of the resulting polymer materials. As the final step, photoinitiated thiol-ene radical addition with multifunctional thiols led to the formation of POETE networks (**3a-f**), which were compared to the simple poly(acetal-thioether) (PATTE, CKA-4TE) network (**4**) formed from the CKA (**1**). The crosslinking density of the resulting networks was controlled by the number of thiol (SH) functionalities on the crosslinker (**3a$_1$-3a$_3$**) and the unsaturated bonds present in the OE precursors (**3e$_2$, 3f$_2$**) that act as additional anchor points.
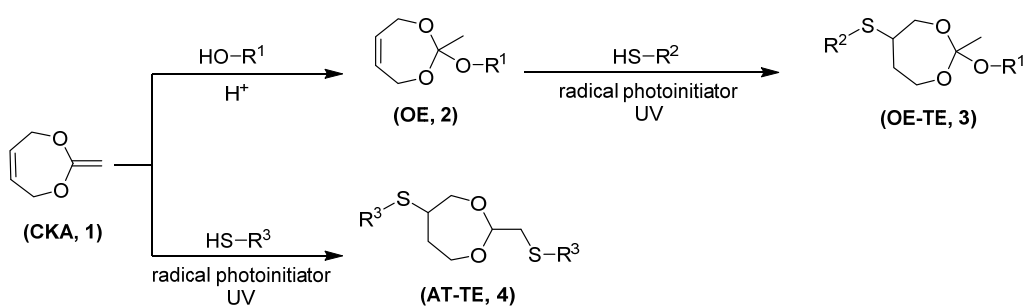
Scheme 1. General synthesis sequence from CKA to OE and OE-TE or AT-TE, respectively, using the radical thiol-ene reaction.
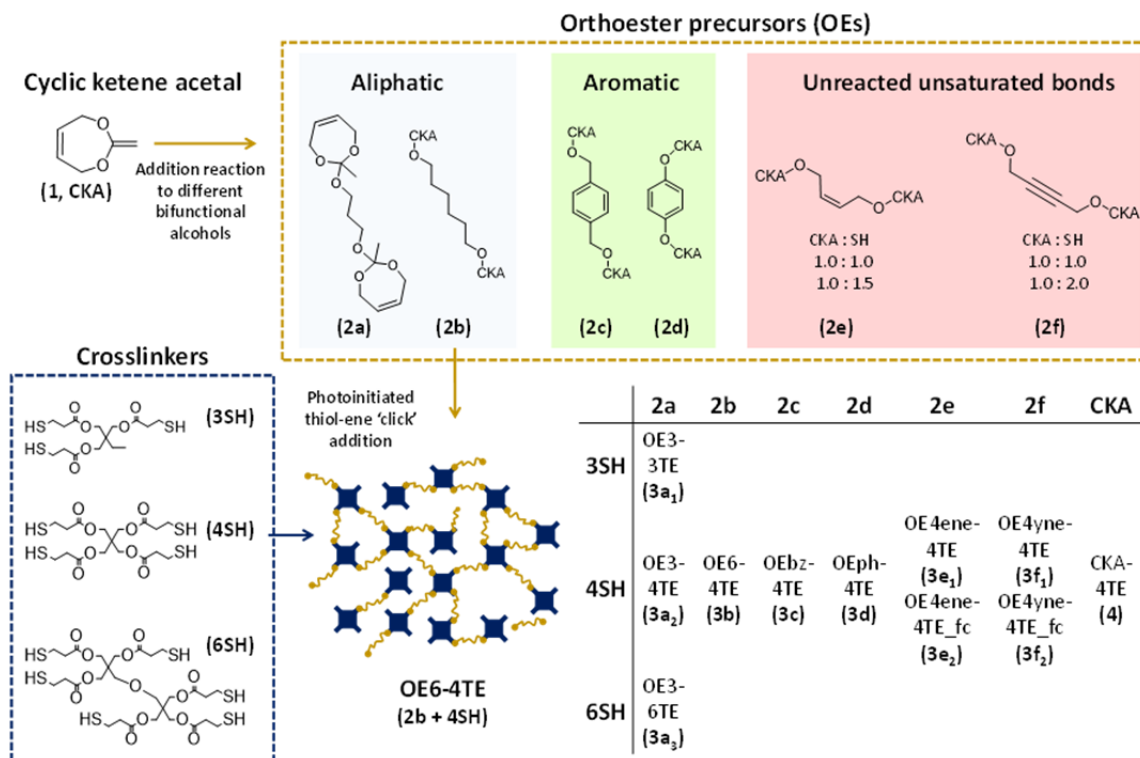
Scheme 2. Synthesis of different OE monomers and composition of all POETE networks formed from the radical thiol-ene reaction. Components of cartoon graphic: multifunctional thiol crosslinkers (**4SH**, blue), bifunctional OE monomer (**OE6**, yellow).

While most of the formulations were liquid at room temperature, the mixtures that contained unsaturated and aromatic compounds (**2c**, **2d**, **2f**) needed to be prepared at elevated temperatures (around 50 °C and 120 °C, respectively) to keep the solutions from solidifying during handling. After addition of a radical photoinitiator (Irgacure 819), exposure of the resin to UV irradiation enabled solidification of the materials. The resulting networks showed extremely rapid surface wetting in contact with air and acidic surfaces, including glass (**Figure S1**), which made them difficult to handle and was likely attributed to incomplete conversion and residual moisture.

**Post-curing strategies and characterization of networks**

Initially focusing on OE3-4TE (**3a₂**), a thermal post-curing at 120 °C under vacuum was undertaken to improve crosslinking and dry the samples. While a significant loss in surface wetting and increase in stiffness was noted during this step, no significant change in the spectra of the materials was observed by IR and Raman spectroscopy (**Figure S2**). This indicated that high conversion was reached after UV irradiation, which confirms the efficient nature of the thiol-ene coupling step.[43] An optimal thermal post-curing time of 120 h was established by DMTA analysis: after such amount of time, a plateau in Loss and Storage Moduli, as well as a maximum in Young's Modulus, respectively, were reached (**Figure 1A**; **Figure S3**).

Interestingly, when the same process was conducted in air, the presence of oxygen during the thermal post-curing step had a significant effect on the samples. Most obviously, this process resulted in different levels of discoloration in the materials (**Figure S4**). Contrary to the initial expectation of oxidation to the sulfoxide or sulfone, XPS analyses (**Figure S5** and **Table S1**) were unable to establish a significant difference in the surface structure from the initial to either vacuum or air post-cured materials, which may be because of the low penetration depth of the technique and immediate oxidation of exposed surfaces. Despite this result, it seems likely that conducting the post-curing process in air at elevated temperatures will have increased the level of sulfoxide or sulfone throughout the material. Indeed a more obvious difference in consistency and glass transition temperature was observed, as confirmed by DSC and DMTA analyses (**Figure 1B**; **Figure S6**). It should be noted that, apart from the known discrepancy between static and dynamic T_g measurements, the difference between temperatures calculated from DSC and DMTA could derive from the difference in heat diffusion through the respective samples, heating rate and structural factors; accordingly, only values of the same techniques were compared. Significant discrepancies of up to 35 °C were discovered for both aliphatic and aromatic compositions between samples post-cured in air or

vacuum, whereas highly unsaturated bond containing networks and PATTE (**4**) were less significantly affected by exposure to oxygen. This difference indicates that aerobic treatment causes a structural change in the network, which could range from oxidation or molecular rearrangements to partial degradation. Consequently, two separate post-curing strategies were followed throughout the manufacturing process in order to characterize the full range of possible materials: one set was cured under vacuum, while the other was left exposed to air, for 120 h at 120 °C each. Furthermore, it should be noted that all T_gs with values between −15 and 45 °C are rather low compared to the glassy or semi-solid POEs reported by Heller and coworkers[44], which ranged between 20 and 100 °C depending on the crystalline content. Hence, all mechanical analyses were conducted at 37 °C to improve reproducibility and simulate physiological conditions.
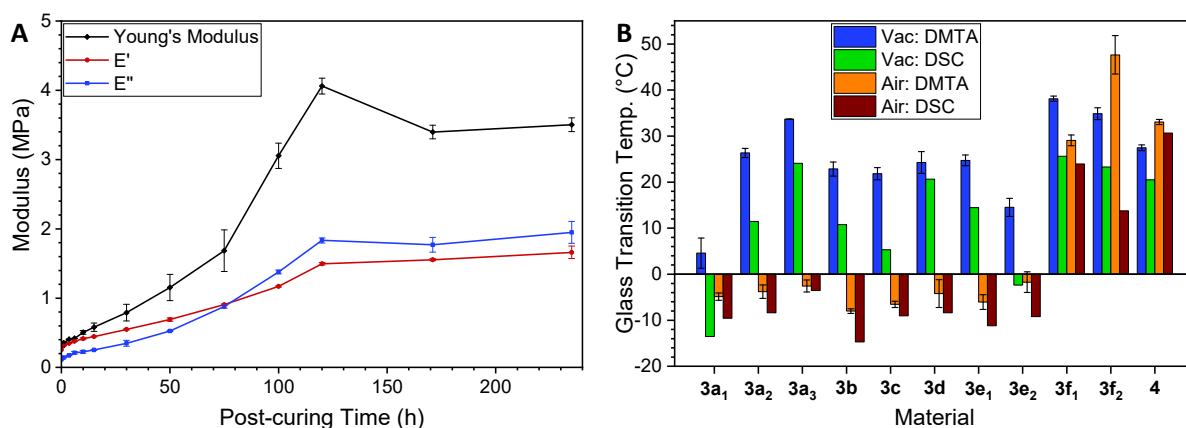
Figure 1. (A) Young's, storage and loss modulus for OE3-4TE (**3a$_2$**) obtained *via* DMTA at different time points after post-curing at 120 °C and $5 \cdot 10^{-2}$ mbar (37 °C, frequency 1 Hz, amplitude 1 to 100 μm, step size increased exponentially; displayed moduli as average over entire data range). (B) Glass transition temperatures obtained from DMTA and DSC temperature sweeps of all network materials (**3a$_1$-4**) after post-curing under vacuum and in air (DMTA: frequency 1 Hz, amplitude 5 μm, 2 K·min^{-1}; DSC: 10 K·min^{-1}).
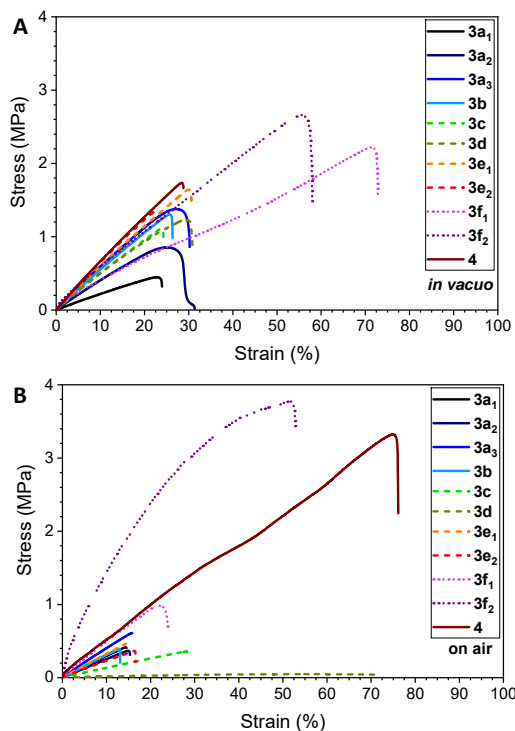
Figure 2. Representative tensile strain-stress curves of all network materials (**3a₁-4**) after post-curing under vacuum (A) and in air (B) (4 mm·min⁻¹, 37 °C).

As a general trend, the vacuum-treated materials (**3a₁-4**) showed a moderate ultimate strain of between 25 and 30%, up to 55 to 70% for the unsaturated species (**3f**), with an ultimate tensile strength (UTS) in a range between 0.4 and 2.6 MPa during tensile testing (**Figure 2**, A and B; **Figure S7**). This behavior is plausible for crosslinked networks above their glass transition temperature. While this specific mechanical strength is low in comparison to the full scope of elastomers, it constitutes a significant improvement compared to original POEs as reported by Heller and coworkers[44], which were either glassy and brittle (e.g. elongation to yield below 15% with UTS of around 35 MPa) or semi-solid gels at relevant temperatures. In contrast, a decrease in ultimate strain by almost half was observed for most samples when subjected to air instead, combined with a general weakening of the elastic modulus as characterized by a decrease in slope. In conjunction with analogous Young's modulus calculations from oscillatory and tensile DMTA (**Figure 1**, E and F; **Figure S8**), the superior

22

mechanical performance of the vacuum-treated materials is clearly established, which suggests a side reaction under oxygen exposure, potentially by oxidation of thioethers or other functional groups. It should be noted that the POETE with the highest crosslinking density (**3f$_2$**) and PATTE (**4**) exhibited high mechanical strength and were less susceptible to oxidation than the other materials studied. Interestingly, the OEph-4TE (**3d**) based on hydroquinone was most affected by the contact with oxygen and turned into a gel, which could be attributed to the highly polar nature of the OE, facilitating oxidation. Therefore, considering the influence of linkers and crosslinkers on the material performance and the previous observations, the vacuum-treated samples were used as main reference.
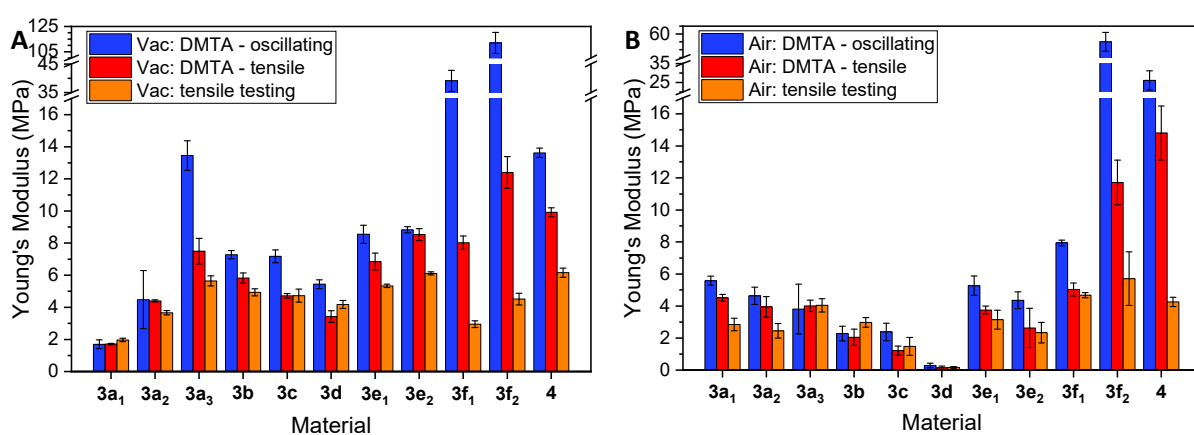
Figure 3. Young's modulus obtained from DMTA measurements in tensile and oscillatory mode as well as from tensile testing curves of networks (**3a$_1$-4**) after post-curing under vacuum (A) and in air (B) (DMTA oscillatory: frequency 1 Hz, amplitude 5 to 100 μm, step size 5 μm; DMTA tensile: 0.1 to 4 N, 0.2 N·min^{-1}; tensile testing: 4 mm·min^{-1}; all measurements at 37 °C).

Higher crosslinking density (**3a$_1$-3a$_3$**) showed a greater effect on mechanical performance than stiffer linker structure (**3b-d**), according to dynamic Young's Moduli (**Figure 3**, A) and related parameters at thermal equilibrium and constant amplitude (**Figure S9**), as well as ultimate tensile stresses (**Figure 2**, A). This could be explained by the low impact of only

three additional methylene groups on chain flexibility, whereas bulky aromatic groups interfere with the network and at the same time are too restricted to coordinate between each other. Similarly, the incorporation of alkene groups (**3e**) did not significantly alter the material properties, probably because the linker is too small to contribute significant stiffness to the network and even gains flexibility upon further crosslinking. The alkyne-linked materials (**3f**), however, exhibited the highest mechanical performance of all POETEs, which could be attributed to the stiffest linker structure and highest crosslinking density, as well as generally the highest glass transition temperature. Indeed, such features render segments sterically hindered, thus locking the structure in place, which even outperformed the PATTE network (**4**).

Degradation studies

In order to investigate the effect of functional groups and crosslinking density on the degradability of the networks, the weight loss of cylindrical samples over time was monitored in 0.1 M HCl (pH = 1.0), 0.1 M NaOH (pH = 13.0) and 1 M PBS solution (pH = 7.4) (**Figure 4**, A and B).
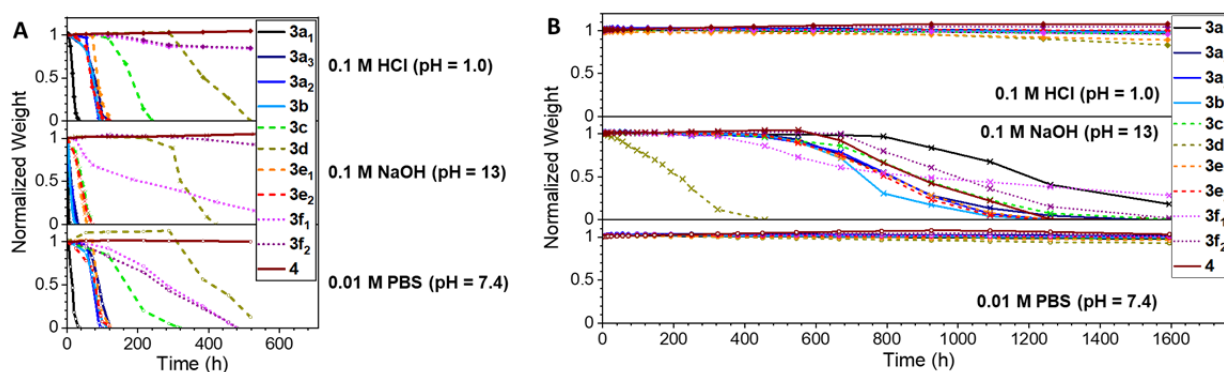

Figure 4. Average relative weight progress over time of POETE (**3a-f**) and PATTE (**4**) network samples after thermal post-curing under vacuum (A) and in air (B) in aqueous media

at 37 °C. Top: 0.1 M HCl (pH = 1.0), center: 0.1 M NaOH (pH = 13.0), bottom: 0.01M PBS buffer solution (pH = 7.4).

While the air-exposed POETE samples (**3a-f**) generally showed virtually no degradation in acidic and neutral media, a slow degradation in basic medium was observed for all samples, including the PATTE (**4**). This indicates that for materials cured under aerobic conditions and subjected to aqueous solutions, a rearranged network structure under loss of orthoester functionalities or oxidation products likely prevented access to the remaining hydrolysable orthoester groups. Furthermore, the selective alkaline erosion suggests a variation in the degradation mechanism under such conditions, for example the neutralization of carboxylated species, which renders the network more hydrophilic and increases the diffusion of water into the material. In contrast, most *in vacuo* treated samples started to degrade within hours until complete dissolution up to 3 weeks later, which is expected if the effect of orthoester groups is dominating. Surprisingly, the samples in alkaline solution showed again the highest degradation rates, with all aliphatic-containing samples (**3a-c, 3e**) fully degrading after up to 4 days. While a detailed mechanism for acidic degradation of POEs can be proposed based on previous studies (**Figure S10**),[35] OEs are generally considered more stable under alkaline conditions. Nevertheless, the OE functionality chemically constitutes a multi-ester with degradation progressing in stepwise hydrolysis and hence both non-trivial acidic and alkaline hydrolysis mechanisms apply, with both rates highly accelerated by either autocatalysis or neutralization of acidic degradation products. The increased degradation rate of aliphatic components could be ascribed to the higher segment mobility of the samples, which would enable higher water diffusion and is most obvious in the almost instantly degrading OE3-3TE (**3a$_1$**) with the lowest crosslinking density. In both acidic and neutral media, a delayed onset of around one day is observed. Similar to the higher determined mechanical strength and glass transition temperature (**Figure 1, 2** and **3**), OE4yne-4TE species (**3f$_1$, 3f$_2$**) showed the greatest

stability in all media, especially under acidic conditions, most likely as a result of the dominating steric hindrance and hydrophobicity. This performance is only surpassed by PATTE (**4**), which remains stable under all conditions. OEph-4TE (**3d**) should again be noted as a special case which exhibits an even more delayed onset, followed by rapid degradation and constant colored release of presumably hydroquinone. While the degradation mixture was complex and hence challenging to identify the remaining components, it is likely that hydrolysis of the orthoester lead to acetic acid and alcohol moieties possibly alongside ester hydrolysis of the crosslinker. Most notably, all degradations are characterized by a linear mass loss, which could indicate surface erosion of the materials.
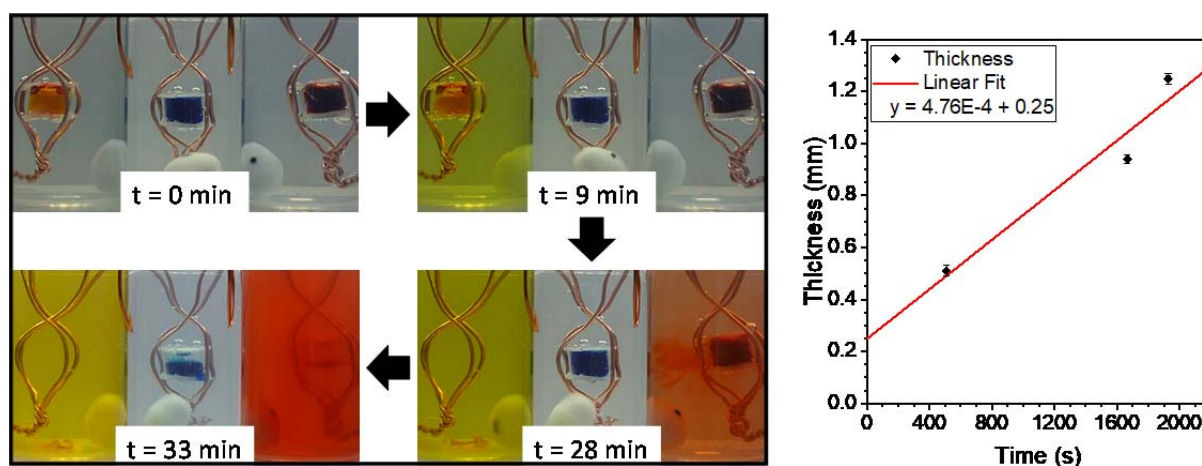
Figure 5. Video frames (left) and initial thickness versus release time diagram (right) documenting the dye release from filled cylinders of OE3-4TE (**3a$_2$**) virgin material in 1 M HCl (pH = 0) at 22 °C. Time points obtained *via* video analysis from onset of HSI (Hue-Saturation-Intensity) value change.

A simple potential application of the rapidly degrading virgin material (see end of section "Synthesis and Preparation", as well as **Figure S1**) was demonstrated *via* erosion studies (**Figure 5**), mimicking programmed delivery or protective coatings of varying thickness.

Although basic media afforded the fastest degradation kinetics, the degradation products were insoluble, leading to turbidity in alkaline or neutral solution and complicating analysis. Therefore, acidic media (1 M HCl, pH = 0) was used for the studies since it was determined to provide adequate degradation rates and good product solubility. Hollow cylinders were created in a scaffold made of clear outer and inner tubing, with the latter of 3 different outer diameters to achieve different wall thickness. The resin was inserted and cured under UV light. Following removal of the tubing, the obtained cylinders were glued to silanized glass plates and filled with undiluted yellow, red or blue food coloring in the order of increasing wall thickness. Other dyes and chromophores were initially screened, but the simple food dyes performed well for the intended purpose. Upon exposure to degradation conditions, no color change resulted from release of encapsulated dye until a bulk release event after several minutes. Release times were determined by video color analysis (**Figure 5** and **Figure S11**) and found to be in a roughly linear relationship with the shell thickness. The intercept of 0.25 mm can be seen as both a minimum layer thickness and a reasonable indication of the critical dimension calculated by Burkersroda *et al.*,[22] where they determined a higher value of 0.6 mm for their linear polyorthoesters as opposed to the here investigated less penetrable network.
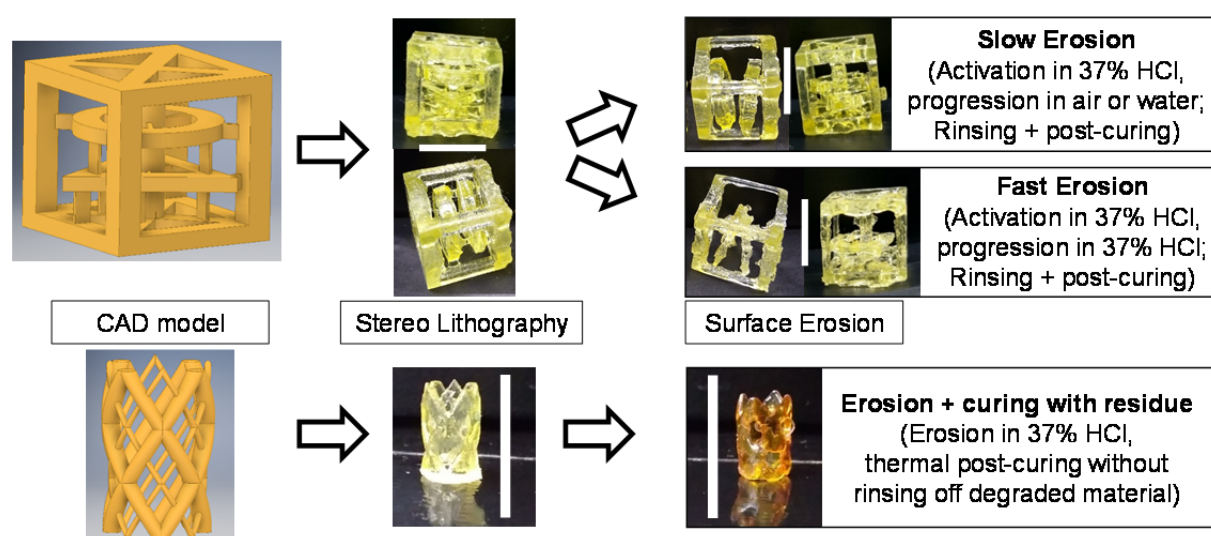
Figure 6. Schematic of the manufacturing and erosion process including 3D models and photographs of a 3D-printed cuboid construct incorporating a suspended circular and triangular component (top) and stent model (bottom) made of OE3-4TE (**3a$_2$**). Scale bar: 1 cm.

As a final manufacturing step, the suitability of the materials for 3D printing and biomedical applications was explored using OE3-4TE (**3a$_2$**) as the model material. After optimization of the resolution and layer thickness, a 3D printing mixture was prepared containing propylene carbonate (33 wt%) as a non-reactive diluent to obtain optimal printing viscosity, the photoinitiator (Irgacure 819, 0.5 wt%) and paprika extract as the photoinhibitor (0.5 wt%). Two different models were designed and printed on a Miicraft 50x in order to demonstrate the versatility of the material and its unique degradation behavior (**Figure 6**). Both structures were post-cured under vacuum at 120 °C for 120 h to ensure complete conversion and long-term stability for storage. Subsequently, the models were eroded starting with an activation step by submerging in concentrated acidic medium (37% (12 M) HCl) for several minutes to accelerate surface erosion and remove passivating oxidized layers, followed by rinsing with water. Thereupon, either slow continuous ambient surface erosion in air or accelerated erosion by re-submersion in 37% HCl was allowed to proceed for several minutes and the final shape was consolidated by drying *in vacuo* at 120 °C for several hours (**Figure 6**, Surface Erosion). The printed cuboid construct (**Figure 6**, top) incorporated two components on thin supporting beams, which were released as trapped mobile parts after surface erosion. Expectedly, the rapidity of the erosion process determined the uniformity of the printed parts; hence, a better-defined structure was obtained from slow erosion in air rather than continued erosion in concentrated acid. In contrast, a stent model (**Figure 6**, bottom) consisting of strands of two different diameters resulted in an initial model without

pores as a consequence of surface tension in the resin. After rapid surface erosion a porous scaffold was obtained. In this case, thermal post-curing of the structure was conducted with a layer of degradation products still present, as its removal could have damaged the fragile structure, which resulted in stronger discoloration as apparently a thick passivating layer was formed.

Cytocompatibility of degradation products

Finally, the cytotoxicity of the material was investigated. Because of the fast degradation of the system in aqueous solutions at 37 °C and its auto-fluorescence, seeding cells on the surface of a specimen was unsuccessful, and thus the determination of its cytotoxicity by a 2D cell experiment on the scaffold was hindered. Hence, the cytocompatiblity of the degradation products was assessed by determining the relative viability of NOR-10 cells after being exposed to cell culture media that contained different concentrations of the 3D printed material (*i.e.* from 0.63 to 20 mg·mL^{-1}).
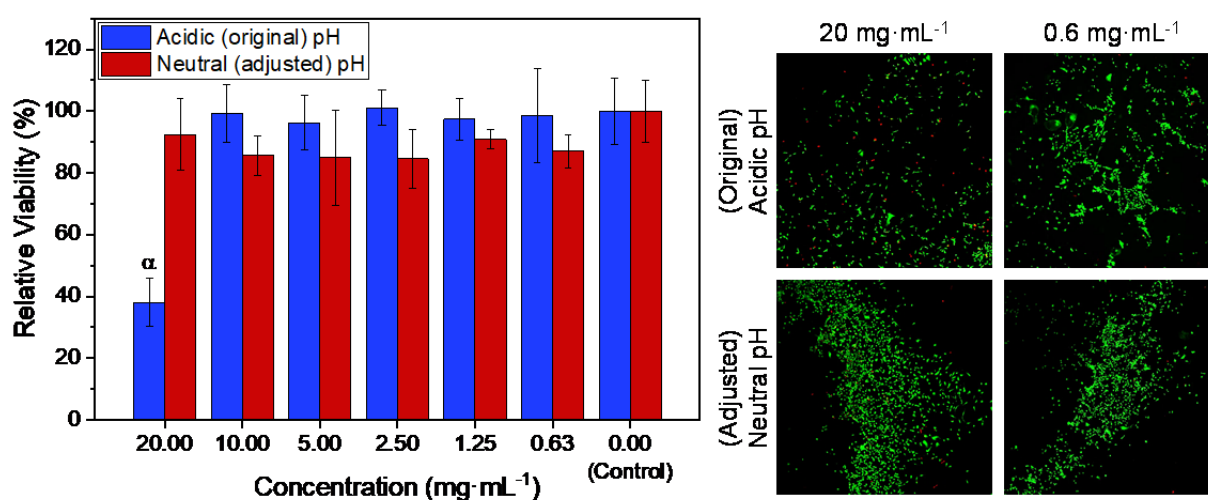
Figure 7. Statistical and fluorescence microscopic representation of the findings from cytotoxicity studies in media containing the degradation products of printed OE3-4TE (**3a$_2$**). Left: Metabolic activity of NOR-10 cells exposed for 48 h to cell culture media with increasing concentration of sample without pH adjustment (blue) and after increasing the pH

by adding NaOH (red). Cell viability in % relative to control. Error bars: SD with n = 3. α on bar refers to significant differences (p-value <0.05): α vs all. Right: Representative live/dead images of cells after being exposed to cell culture media containing 20 mg·mL^{-1} (left column) and 0.6 mg·mL^{-1} (right column) of sample with (top) and without (bottom) pH adjustment. Image size 3.5 × 3.5 mm.

For that purpose, samples of the 3D printed models were taken after activation, rinsed and left to degrade in cell medium. Then, NOR-10 cells were exposed to those cell media. After 48 h of incubation, the cell viability at a concentration of 20 mg/mL (38%) was significantly lower in comparison to lower concentrations (**Figure 7**). Accordingly, the cell viability was recovered (99%) after diluting the cell media (10 mg·mL^{-1}) and remained higher than 96% for the rest of conditions tested. *A priori*, we attributed the decrease in cell viability to the acidic pH (6.5) caused by the POETE degradation products, with a plausible release of acetic acid and diol compounds. Indeed, when the pH of the cell culture solutions was increased to around 7.5 by adding 10 uL NaOH 1 M, the cell viability was determined to be higher than 84% regardless of the sample concentration and comparable to the control (*i.e.* original cell culture medium). Additional live-dead fluorescent staining supported these results (**Figure 7**; **Figure S12**). Consequently, future studies of design and application of POETE devices *in vivo* have to take in account the resulting environmental acidity as a function of surface area and degradation rate. It is worth noting that commonly used PLA-based implants also share this issue but the apparent surface eroding nature of the present materials will enable a more gradual release of acid-containing species than the bulk eroding polyester materials that may enable the acidic byproducts to be readily transported and diluted before complications such as acidosis occur. Therefore, future works can focus on tuning the composition of the 3D

printed scaffolds to include pH-adjusting compounds to be released during degradation, thus maintaining a neutral pH harmless to cells and tissue.

CONCLUSIONS

In conclusion, surface-erodible POETE and PATTE networks with enhanced performance have been added to the library of suitable resources for AM applications. Specifically, these new polymer systems display a broad spectrum of thermo-mechanical properties under physiological conditions that depend on the linker structure and crosslinking density, generally outperforming those previously reported for orthoester-containing homopolymers. Similarly, regarding their tailored degradation profile, degradation rates in aqueous media varied from complete surface erosion within days up to several months without mass loss. Furthermore, as a test for drug delivery applications, the delayed bulk-release of dyes on a representative material was demonstrated. As POETEs were successfully 3D printed, we envisage the subsequent surface erosion of the resulting device to be exploited for controlled fading of support structures. Although cytocompatibility investigations were complicated as a consequence of the rapid surface erosion of the device, the degradation products were proved to be nontoxic for cells, either with pH regulation or below a certain concentration, thus resembling currently used biomedical materials. Overall, POETE networks show great potential for future applications as biomedical materials based on the combination of customizable mechanical properties, surface-erosion and their suitability for 3D printing techniques.

SUPPORTING INFORMATION

Photographs of $3a_2$ virgin material samples on an untreated glass surface in air at t = 0 d (initial), 2 d and 4 d; IR and Raman absorption spectra of $3a_2$ formulations and materials after

different times of thermal post-curing in vacuo; Strain-stress curves of 3a$_2$ materials after different times of thermal post-curing in vacuo obtained from dynamic mechanical thermal analysis; Photographs of assorted samples of all materials (3a1-4) after post-curing; X-ray Photoelectron Spectra (XPS) of 3a$_2$ samples before (virgin) and after post-curing; Assignments and fitted numerical composition of molecular environments and XPS binding energy of 3a$_2$ samples before (virgin) and after post-curing; Thermograms of samples of all materials (3a$_1$-4) obtained from DMTA, DSC and TGA after post-curing; Strain-stress curves of all materials (3a$_1$-4) obtained from tensile testing at 37 °C after post-curing; Peak strain, stress and elastic modulus values including standard deviation of all materials (3a$_1$-4) obtained from tensile testing at 37 °C after post-curing; Strain-stress curves of all materials (3a$_1$-4, 3 curves each) obtained from DMTA at 37 °C after post-curing; Loss and storage modulus, dissipation factor tan δ and stress of all materials (3a$_1$-4) obtained from DMTA at 37 °C and constant amplitude after post-curing; Potential stepwise acidic hydrolysis mechanism involving OE functionalities; Color intensity and saturation of aqueous media surrounding dye-filled cylinders of 3a$_2$ obtained from video analysis over time; Live/dead images of cells before and after being exposed to cell culture media containing different concentrations of sample with and without pH adjustment; ^{1}H NMR spectra and structural assignment of all employed OE monomers (2a-2f); ^{13}C NMR spectra and structural assignment of all employed OE monomers (2a-2f); IR and Raman absorption spectra of all employed OE monomers (2a-2f) and network materials (3a$_1$-4) after post-curing.

AUTHOR INFORMATION

Corresponding Author

Andrew P. Dove - *School of Chemistry, University of Birmingham, Edgbaston, Birmingham, B15 2TT, UK; Email: A.Dove@bham.ac.uk*

Authors

Gordon Herwig - *Department of Chemistry, University of Warwick, Coventry, CV8 4AL, UK; School of Chemistry, University of Birmingham, Edgbaston, Birmingham, B15 2TT, UK; Laboratory for Advanced Fibers, Empa - Swiss Federal Laboratories for Materials Testing and Research, Lerchenfeldstrasse 5, 9014 St. Gallen, CH*

Maria M. Pérez-Madrigal - *School of Chemistry, University of Birmingham, Edgbaston, Birmingham, B15 2TT, UK;*

Notes

The authors declare no competing financial interest.

REFERENCES

(1) Kruth, J.-P.; Leu., M. C.; Nakagawa, T., Progress in additive manufacturing and rapid prototyping. *CIRP Ann. Manuf. Technol.* **1989,** *47* (2), 525-540.

(2) Gibson, I.; Rosen, D.; Stucker, B., *Additive manufacturing technologies*. Springer New York: 2015.

(3) Lim, S.; Buswell, R. A.; Le, T. T.; Austin, S. A.; Gibb, A. G. F.; Thorpe, T., Developments in construction-scale additive manufacturing processes. *Autom. Constr.* **2012,** *21*, 262–268.

(4) Rengier, F.; Mehndiratta, A.; von Tengg-Kobligk, H.; Zechmann, C. M.; Unterhinninghofen, R.; Kauczor, H. U.; Giesel, F. L., 3D printing based on imaging data: Review of medical applications. *Int. J. Comput. Assist. Radiol. Surg.* **2010,** *5* (4), 335-41.

(5) Melchels, F. P. W.; Domingos, M. A. N.; Klein, T. J.; Malda, J.; Bartolo, P. J.; Hutmacher, D. W., Additive manufacturing of tissues and organs. *Prog. Polym. Sci.* **2012,** *37* (8), 1079–1104.

(6) Wendel, B.; Rietzel, D.; Kühnlein, F.; Feulner, R.; Hülder, G.; Schmachtenberg, E., Additive Processing of Polymers. *Macromol. Mater. Eng.* **2008,** *293* (10), 799-809.

(7) Petrovic, V.; Vicente Haro Gonzalez, J.; Jordá Ferrando, O.; Delgado Gordillo, J.; Ramón Blasco Puchades, J.; Portolés Griñan, L., Additive layered manufacturing: sectors of industrial application shown through case studies. *Int. J. Prod. Res.* **2010,** *49* (4), 1061-1079.

(8) Gebhardt, A., *Understanding additive manufacturing*. Carl Hanser Verlag GmbH & Co. KG: Munich, Germany, 2011; p 173.

(9) Popescu, D.; Laptoiu, D., Rapid prototyping for patient-specific surgical orthopaedics guides: A systematic literature review. *Proc. Inst. Mech. Eng. H J. Eng. Med.* **2016,** *230* (6), 495-515.

(10) Arcaute, K.; Mann, B. K.; Wicker, R. B., Stereolithography of three-dimensional bioactive poly(ethylene glycol) constructs with encapsulated cells. *Ann. Biomed. Eng.* **2006,** *34* (9), 1429-1441.

(11) Barker, I. A.; Ablett, M. P.; Gilbert, H. T. J.; Leigh, S. J.; Covington, J. A.; Hoyland, J. A.; Richardson, S. M.; Dove, A. P., A microstereolithography resin based on thiol-ene chemistry: towards biocompatible 3D extracellular constructs for tissue engineering. *Biomater. Sci.* **2014,** *2* (4), 472-475.

(12) Cooke, M. N.; Fisher, J. P.; Dean, D.; Rimnac, C.; Mikos, A. G., Use of stereolithography to manufacture critical-sized 3D biodegradable scaffolds for bone ingrowth. *J. Biomed. Mater. Res., Part B* **2003,** *64B* (2), 65-69.

(13) Griffin, J.; Delgado-Rivera, R.; Meiners, S.; Uhrich, K. E., Salicylic acid-derived poly(anhydride-ester) electrospun fibers designed for regenerating the peripheral nervous system. *J. Biomed. Mater. Res., Part A* **2011,** *97A* (3), 230-242.

(14) Hutmacher, D. W.; Schantz, J. T.; Lam, C. X. F.; Tan, K. C.; Lim, T. C., State of the art and future directions of scaffold-based bone engineering from a biomaterials perspective. *J. Tissue Eng. Regen. Med.* **2007,** *1* (4), 245-260.

(15) Jungst, T.; Smolan, W.; Schacht, K.; Scheibel, T.; Groll, J., Strategies and molecular design criteria for 3D printable hydrogels. *Chem. Rev.* **2016,** *116* (3), 1496-1539.

(16) Leigh, S. J.; Gilbert, H. T. J.; Barker, I. A.; Becker, J. M.; Richardson, S. M.; Hoyland, J. A.; Covington, J. A.; Dove, A. P., Fabrication of 3-dimensional cellular constructs via microstereolithography using a simple, three-component, poly(ethylene glycol) acrylate-based system. *Biomacromolecules* **2013,** *14* (1), 186-192.

(17) Mota, C.; Puppi, D.; Chiellini, F.; Chiellini, E., Additive manufacturing techniques for the production of tissue engineering constructs. *J. Tissue Eng. Regen. Med.* **2015,** *9* (3), 174-190.

(18) Probst, F. A.; Hutmacher, D. W.; Muller, D. F.; Machens, H. G.; Schantz, J. T., Calvarial reconstruction by customized bioactive implant. *Handchir. Mikrochir. Plast. Chir.* **2010,** *42* (6), 369-373.

(19) Youssef, A.; Hollister, S. J.; Dalton, P. D., Additive manufacturing of polymer melts for implantable medical devices and scaffolds. *Biofabrication* **2017,** *9* (1), 012002.

(20) Ulery, B. D.; Nair, L. S.; Laurencin, C. T., Biomedical applications of biodegradable polymers. *J. Polym. Sci. B. Polym. Phys.* **2011,** *49* (12), 832-864.

(21) Shoichet, M. S., Polymer scaffolds for biomaterials applications. *Macromolecules* **2010,** *43* (2), 581-591.

(22) von Burkersroda, F.; Schedl, L.; Gopferich, A., Why degradable polymers undergo surface erosion or bulk erosion. *Biomaterials* **2002,** *23* (21), 4221-31.

(23) Burkoth, A. K.; Burdick, J.; Anseth, K. S., Surface and bulk modifications to photocrosslinked polyanhydrides to control degradation behavior. *J. Biomed. Mater. Res., Part A* **2000,** *51* (3), 352-359.

(24) Kumar, N.; Langer, R. S.; Domb, A. J., Polyanhydrides: An overview. *Adv. Drug Deliv. Rev.* **2002,** *54* (7), 889–910.

(25) Falco, E. E.; Patel, M.; Fisher, J. P., Recent developments in cyclic acetal biomaterials for tissue engineering applications. *Pharm. Res.* **2008,** *25* (10), 2348-2356.

(26) Andriano, K. P.; Tabata, Y.; Ikada, Y.; Heller, J., In vitro and in vivo comparison of bulk and surface hydrolysis in absorbable polymer scaffolds for tissue engineering. *J. Biomed. Mater. Res.* **1999,** *48* (5), 602-12.

(27) Sommerfeld, S. D.; Zhang, Z.; Costache, M. C.; Vega, S. L.; Kohn, J., Enzymatic surface erosion of high tensile strength polycarbonates based on natural phenols. *Biomacromolecules* **2014,** *15* (3), 830-836.

(28) Langer, R., Biomaterials and biomedical engineering. *Chem. Eng. Sci.* **1995,** *50* (24), 4109-4121.

(29) Lee, J. W.; Gardella, J. A., Jr., Surface perspectives in the biomedical applications of poly(alpha-hydroxy acid)s and their associated copolymers. *Anal. Bioanal. Chem.* **2002,** *373* (7), 526-37.

(30) Zou, T.; Cheng, S.-X.; Zhang, X.-Z.; Zhuo, R.-X., Novel cholic acid functionalized star oligo/poly(DL-lactide)s for biomedical applications. *J. Biomed. Mater. Res., Part B* **2007,** *82B* (2), 400-407.

(31) Fisher, J. P.; Vehof, J. W. M.; Dean, D.; van der Waerden, J.; Holland, T. A.; Mikos, A. G.; Jansen, J. A., Soft and hard tissue response to photocrosslinked poly(propylene fumarate) scaffolds in a rabbit model. *J. Biomed. Mater. Res.* **2002,** *59* (3), 547-556.

(32) Pashneh-Tala, S.; Owen, R.; Bahmaee, H.; Rekštytė, S.; Malinauskas, M.; Claeyssens, F., Synthesis, characterization and 3D micro-structuring via 2-photon polymerization of poly(glycerol sebacate)-methacrylate – An elastomeric degradable polymer. *Front. Phys.* **2018,** *6*, Article 41.

(33) Poetz, K. L.; Mohammed, H. S.; Shipp, D. A., Surface eroding, semicrystalline polyanhydrides via thiol–ene "click" photopolymerization. *Biomacromolecules* **2015,** *16* (5), 1650-1659.

(34) Choi, N. S.; Heller, J. Drug delivery devices manufactured from poly(orthoesters) and poly(orthocarbonates). 4093709 A, 1978-6-6, 1978.

(35) Heller, J.; Barr, J.; Ng, S. Y.; Abdellauoi, K. S.; Gurny, R., Poly(ortho esters): Synthesis, characterization, properties and uses. *Adv. Drug Deliv. Rev.* **2002,** *54* (7), 1015-1039.

(36) Dutta, D. 2003, Biodegradable stent of a polyorthoester polymer or a polyanhydride polymer. US8414642B2.

(37) Haider, T.; Shyshov, O.; Suraeva, O.; Lieberwirth, I.; von Delius, M.; Wurm, F. R., Long-chain polyorthoesters as degradable polyethylene mimics. *Macromolecules* **2019,** *52* (6), 2411-2420.

(38) Tschan, M. J. L.; Ieong, N. S.; Todd, R.; Everson, J.; Dove, A. P., Unlocking the potential of poly(ortho ester)s: A general catalytic approach to the synthesis of surface-erodible materials. *Angew. Chem. Int. Ed.* **2017,** *56* (52), 16664-16668.

(39) Fu, S.; Yang, G.; Wang, J.; Wang, X.; Cheng, X.; Tang, R., Acid-degradable poly(ortho ester urethanes) copolymers for potential drug carriers: Preparation, characterization, in vitro and in vivo evaluation. *Polymer* **2017,** *114*, 1-14.

(40) Wei, B.; Tao, Y.; Wang, X.; Tang, R.; Wang, J.; Wang, R.; Qiu, L., Surface-eroding poly(ortho ester amides) for highly efficient oral chemotherapy. *ACS Appl. Mater. Interfaces* **2015,** *7* (19), 10436-10445.

(41) Herwig, G.; Dove, A. P., Synthesis of rapidly surface eroding polyorthoesters and polyacetals using thiol-ene click chemistry. *ACS Macro Lett.* **2019,** *8* (10), 1268-1274.

(42) Plikk, P.; Tyson, T.; Finne-Wistrand, A.; Albertsson, A. C., Mapping the characteristics of the radical ring-opening polymerization of a cyclic ketene acetal towards the creation of a functionalized polyester. *J. Polym. Sci. A. Polym. Chem.* **2009,** *47* (18), 4587-4601.

(43) Barner-Kowollik, C.; Du Prez, F. E.; Espeel, P.; Hawker, C. J.; Junkers, T.; Schlaad, H.; Van Camp, W., "Clicking" polymers or just efficient linking: What is the difference? *Angew. Chem. Int. Ed.* **2011,** *50* (1), 60-62.

(44) Daniels, A. U.; Andriano, K. P.; Smutz, W. P.; Chang, M. K. O.; Heller, J., Evaluation of absorbable poly(ortho esters) for use in surgical implants. *J. Appl. Biomater.* **1994,** *5* (1), 51-64.

TOC graphic